How to suppress radiative losses in high-contrast integrated Bragg gratings

Manfred Hammer, Henna Farheen, and Jens Förstner*

Theoretical Electrical Engineering, Paderborn University, Paderborn, Germany

Abstract: High-contrast slab waveguide Bragg gratings with 1-D periodicity are investigated. For specific oblique excitation by semi-guided waves at sufficiently high angles of incidence, the idealized structures do not exhibit any radiative losses, such that reflectance and transmittance for the single port mode add strictly up to one. We consider a series of symmetric, fully and partly etched finite gratings, for parameters found in integrated silicon photonics. These can act as spectral filters with reasonably flat-top response. Apodization can lead to more box shaped reflectance and transmittance spectra. Together with a narrow-band Fabry-Perot filter, these configurations are characterized by reflection bands, or transmittance peaks, with widths that span three orders of magnitude.

Keywords: photonics, integrated optics, waveguide Bragg gratings, 1-D photonic crystals, wavelength filters, bandpass filter, narrow-pass filters, oblique propagation of semi-guided waves.

1 Introduction

Periodically corrugated dielectric optical waveguides, or waveguide Bragg gratings [1–5], are employed, with various purposes and in manifold variants, as fundamental building blocks of current integrated photonic circuits. Wave propagation along finite gratings, if operated in conventional configurations, appears to be always accompanied by more or less pronounced radiative losses [6–8], originating either from the excitation of leaky eigenmodes of the periodic grating, or from the mismatch between the modes supported by the corrugated and non-corrugated waveguide segments. This concerns especially structures with high refractive index contrast and/or large corrugation depths. For certain applications, the out of plane radiation can be seen as a desired and thus specifically tailored feature. Examples are grating couplers for connecting an integrated circuit to optical fibers [9–12], or gratings applied for light extraction from light-emitting sources [13, 14]. In many other circumstances, however, these out-of-plane losses are highly unwanted. Here the list of applications includes various kinds of filters for optical signal processing [4, 15], (refractometric) optical sensors [16–18], or lasers based on waveguide Bragg reflectors [19–21].

Without focusing on any particular application, with this paper we address these latter scenarios. We restrict the discussion to high-contrast gratings with simple rectangular corrugations and 1-D periodicity. Contrary to conventional settings, these are excited by optical waves (semi-guided waves [22, 23]) that are strictly confined in the direction perpendicular to the guiding slab, that have the functional shape of a plane wave with respect to the two in-plane coordinate axes, and that come in to the grating at an oblique angle of incidence. Fig. 1 illustrates this geometry. As we shall argue in Section 2, the oblique excitation makes all the difference: For a sufficiently high angle of incidence, radiation losses, originating either from the corrugated region or from the interfaces between the grating and the original slab, are (mathematically) fully suppressed.

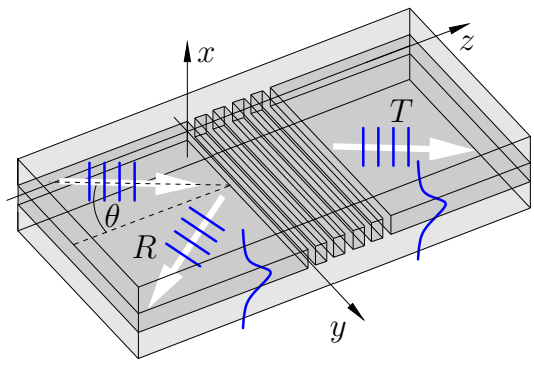

Figure 1: A high-contrast grating in a slab waveguide, schematically. Cartesian coordinates x, y, z are oriented such that x is perpendicular to the slab plane, with the y-axis parallel to the grooves of the grating. Incoming semi-guided waves propagate in the y-z-plane at an angle θ with respect to the grating normal z. Outgoing waves with reflectance R and transmittance T are observed under oblique angles.

*Paderborn University, FG Theoretical Electrical Engineering Warburger Straße 100, 33098 Paderborn, Germany
Phone: ++49(0)5251/60-3560 Fax: ++49(0)5251/60-3524 E-mail: manfred.hammer@uni-paderborn.de

Optics of semi-guided waves can be counted among the earliest concepts of integrated photonics [24–26], at that time with a focus on low refractive index contrast. A series of more recent studies covers 90°-folds in optical slab waveguides [27–29], waveguide facets with a coating segment [30, 31], mirrors [32], the oblique wave propagation across channel waveguides with rectangular [33–42] and circular cross sections [43–45], with direct and evanescent interaction, for the realization of a variety of filtering functions, and for the selective excitation of fiber modes with high-order orbital angular momentum, further the equivalents of diffraction gratings [46, 47], resonant absorbers [48], lenses [49], or composite systems like entire spectrometers [50]. While in all cases the wave propagation in slab waveguides is considered, also components of various types for semi-guided Bloch surface waves have been proposed [51–54].

The present paper picks up a recent discussion of optical beam splitters [55] operating on semi-guided waves in high-contrast dielectric slabs. In the next section 2 we review some more general properties of the systems with oblique excitation [23, 28], specializing things to the present gratings. Sections 2.1–2.3 add brief remarks on the simulation technique, on band structure analysis, and on the oblique excitation by semi-guided beams of limited lateral width. In Sections 3–5 we then discuss a series of computational results for simple fully-etched high contrast gratings without and with apodization, for symmetric partly etched gratings, and finally for a narrow-band filter of Fabry-Perot type.

2 Oblique excitation by the semi-guided fundamental TE-wave

As a starting point for the analysis, we observe that the gratings of Fig. 1 are constant along the y-coordinate parallel to the grooves. This includes the half-infinite access waveguides that extend in $\pm z$-direction. We consider incident waves with the profiles, along the vertical x-axis, of guided modes supported by these slabs. Concerning the propagation in the y-z-plane, these have the functional form of a plane wave coming in at angle θ with respect to the normal to the grooves.

One thus looks for solutions of the full Maxwell equations in the frequency domain with a harmonic y-dependence $\sim \exp(-\mathrm{i}k_y y)$ of all optical electromagnetic fields. The formal equations for this "2.5-D" setting [22, 23, 28, 56] are identical to the equations that govern the modes of dielectric channel waveguides with 2-D cross sections. Here, however, these establish a scattering problem with a common wavenumber

$$k_y = kN_{\text{in}} \sin\theta, \tag{1}$$

determined by the angle of incidence θ, for vacuum wavenumber k and effective index N_{in} of the incoming slab mode. In the first place, the resulting vectorial equations need to be solved on the 2-D cross-sectional x-z-plane, with transparent boundary conditions that accommodate the incoming semi-guided wave.

In the homogeneous regions outside the guiding cores, all electromagnetic field components satisfy a standard 2-D Helmholtz equation [22, 23, 28], but with an effective permittivity

$$\epsilon_{\text{eff}} = n_{\text{b}}^2 - N_{\text{in}}^2 \sin^2\theta \tag{2}$$

in place of the actual permittivity n_{b}^2 of the background medium. In case of excitation by a mode with sufficiently large effective index, and at sufficiently large angle of incidence $\theta > \theta_{\text{b}}$ with $\sin\theta_{\text{b}} = n_{\text{b}}/N_{\text{in}}$, this effective permittivity can become negative. Then these regions do not longer permit any propagating fields: All outgoing optical waves are of evanescent type, and, as such, they do not transport any optical power. Radiative losses are thus fully suppressed.

Alternatively, this can be understood in terms of fairly general results from the more detailed analysis in Refs. [23, 28, 56]. Given the excitation by an incoming wave with effective index N_{in}, a propagating semi-guided outgoing wave with effective index N_{out} is observed at an angle θ_{out} that is related to the angle of incidence θ by an equation in the form of Snell's law:

$$N_{\text{out}} \sin\theta_{\text{out}} = N_{\text{in}} \sin\theta. \tag{3}$$

Hence, for the gratings with single-mode slabs of identical thickness next to the corrugated regions, reflected or transmitted waves of the same polarization propagate at the same angle $\theta_{\text{out}} = \theta$ as the incident wave.

In cases where Eq. (3) does not yield a real angle θ_{out}, the outgoing wave becomes evanescent. This happens, if the structure is excited at angles $\theta > \theta_{\text{cr}}$, for a critical angle θ_{cr} with

$$\sin\theta_{\text{cr}} = N_{\text{out}}/N_{\text{in}}. \tag{4}$$

Non-guided, radiative outgoing waves ("cladding modes") are characterized by effective indices below the level n_{b}, i.e. all these waves become evanescent for excitation at angles $\theta > \theta_{\text{b}}$. We are thus led to the same limiting angle for the suppression of radiative losses as before.

Next we specialize things to the examples in Sections 3–5. Refractive indices of $n_{\text{b}} = 1.45$ for the substrate (or buffer layer) and cover medium and $n_{\text{g}} = 3.45$ for the slab core, a standard film thickness of $d = 220\,\text{nm}$, and interest in a spectral region around the target vacuum wavelength $\lambda = 1.55\,\mu\text{m}$ are typical values for Si/SiO_2 slab waveguides in the field of silicon photonics [57–59]. For reasons of simplicity, we neglect material dispersion. Note, however, that all theoretical arguments and numerical simulations are strictly based on a frequency domain description. Hence, once a particular material model [60, 61] has been agreed upon for a specific realization task, including the effects of material dispersion [7] should be straightforward. Further, for reasons as given in the next paragraphs, we also restrict the discussion to excitation by the fundamental TE mode at a convenient angle of $\theta = 45°$, and to covered structures, i.e. structures that are mirror symmetric with repect to the y-z-plane at $x = 0$ (cf. Figs. 3, 9, 12).

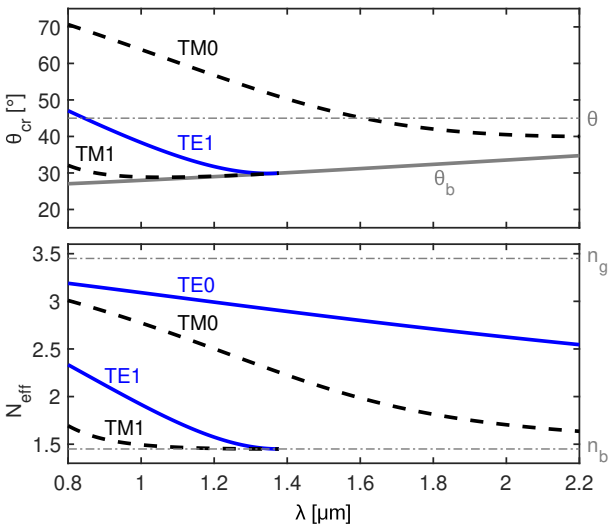

Figure 2: Bottom: Effective indices N_{eff} of the guided modes of a symmetric slab waveguide of thickness $d = 0.22\,\mu\text{m}$, with refractive index contrast $n_b : n_g = 1.45 : 3.45$, as a function of the vacuum wavelength λ. TE- (solid) and TM-polarized (dashed) modes of fundamental (TE_0, TM_0) and first order (TE_1, TM_1) are supported. Top: Critical angles θ_{cr} (Eq. (4)) associated with the TM_0-, TE_1-, and TM_1-modes, and the critical angle θ_b for propagating waves supported by the background medium, for excitation by the TE_0-mode. A horizontal line marks the angle of incidence of $\theta = 45°$ used for all configurations in this paper.

Along with the modal effective indices [62], the former critical angles change with the vacuum wavelength of the incident light. Fig. 2 summarizes these values, for the parameters considered in the later examples. Besides the fundamental TE_0-mode, the slabs support further guided fields. In principle, the grooves of the gratings must be expected to scatter into these modes, such that mode and/or polarization conversion [28] could occur. There are two mechanisms that prevent these effects.

On the one hand, according to Fig. 2, for TE_0-excitation at $\theta = 45°$ the critical angles (4) for the TM_1, TE_1 (largely), and TM_0 modes (partly) are below the angle of incidence. In the respective spectral regions, the modes become evanescent. On the other hand, referring to the coordinates of Fig. 3, the incident TE_0 wave has a specific mirror symmetry with respect to the plane at $x = 0$. Its vectorial electric and magnetic profile $(\boldsymbol{E}, \boldsymbol{H})$ comprises a vanishing component $E_x = 0$, even components E_y, E_z, and H_x, and odd components H_y and H_z [56]. The TE_0-mode satisfies what is called perfect magnetic conductor (PMC)-boundary conditions [63] at $x = 0$. Since the full structure is also mirror symmetric, this symmetry can be extended to the entire optical electromagnetic field. Contrarily, the TM_0 and TE_1 modes have profiles with even (zero) E_x, odd E_y and E_z, odd (zero) H_x, and even H_y and H_z components; they comply with perfect-electric-conductor (PEC) conditions at $x = 0$. The incoming TE_0 wave can thus not excite these two modes. While this does not hold for the TM_1 mode which is of the same symmetry class as TE_0, its critical angle is below the angle of incidence, and the mode is evanescent, for the full wavelength interval. Note, however, that the former symmetry arguments require strictly vertical sidewalls of the grooves.

In total, just as are the radiative losses, power transfer to any outgoing waves based on the TM_0, TE_1, and TM_1 modes is prohibited for the entire spectral range of interest. For TE_0 excitation, outgoing power is carried by

the reflected and transmitted TE_0-waves only; our model predicts reflectances and transmittances that strictly add up to one.

The symmetry arguments work both ways. For oblique excitation by an incoming TM_0 mode, power transfer to potentially outgoing TE_0-waves with much higher effective index is forbidden [55]. It should thus be possible to adapt the structures of Sections 3–5 for TM polarization, with full suppression of radiative losses and suppression of mode / polarization conversion. This would require a re-dimensioning of the structures, and, with larger critical angles, operation at a higher angle of incidence, in general (not followed up in this paper).

2.1 Simulations by bidirectional eigenmode propagation

The numerical computations in Sections 3–5 can rely on an outwards exponential decay of all electromagnetic fields in the direction x perpendicular to the slab plane. Hence, simulations with "hard", non-transparent boundary conditions, imposed at a sufficient distance from the guiding core, can be used in this case. Our numerical simulations are based on a simulation technique as described in [8, 56, 64, 65]. The semianalytical frequency-domain solver addresses the 2.5-D scattering problem on a 2-D computational domain with transparent-influx boundary conditions (or externally unbounded homogeneous regions) at the left and right edges of a horizontal (z-) interval, and with boundary conditions of Dirichlet type at the lower and upper edges of a vertical (x-) computational interval. The scheme relies on bidirectional expansions into polarized local vectorial slab eigenmodes propagating along the horizontal z-coordinate (vectorial bidirectional eigenmode propagation, BEP).

These are fully vectorial simulations of high-contrast dielectric structures with discontinuous permittivity. Approximations of narrow, peaked (divergent) features in the fields at the edges and corners of the grooves are required, just as in standard calculations of modes of rectangular dielectric waveguides. Besides the TE terms, also the TM-polarized elements of the set of basis slab-modes are necessary for convergence of the simulations. Note that, even if the TM and higher order TE fields do not transport any optical power, these slab modes can well play a role in the local representations of the optical electromagnetic fields in the corrugated grating region.

The domain size along x and the number of expansion terms enter as computational parameters, where the values required for convergence may depend on the particular configurations encountered in a (wavelength) sweep. The previous theory predicts strictly power conservative gratings, with unit sum of reflectance R and transmittance T, where the actual power balance realized by the numerical approximations can serve as an indicator for convergence. With x-intervals with margins of $[0.6, 0.8]\,\mu$m or $[0.6, 0.8]\lambda$ above and below the upper and lower core interface, and typically about 120 expansion terms per polarization (numbers ranging from 30 (band structure) to 250 (long finite gratings, spectral regions at the band edges)), we observed deviations $|R + T - 1|$ of less than 0.01 for all simulations that led to the data as displayed.

2.1.1 Numerical finite element simulations

The rigorous finite-element (FE) solvers in the COMSOL multiphysics suite [66] also cover the present parameterized 2-D problems. We applied these tools for a corroboration of the BEP results; respective data has been included in Figs. 5(b) and 11(b). Excellent agreement is observed.

2.2 Band structure calculations

As a means of characterizing the interior part of the gratings, one analyses the respective infinite periodic structure, here for the propagation of waves that are generated by the oblique excitation process. To that end, we look for solutions of Maxwell equations in the form of (Floquet-) Bloch modes [1,2,67]. Assuming a frequency domain representation with time dependence $\sim\exp(\mathrm{i}\omega t)$ of all fields for frequency $\omega = k\mathrm{c} = 2\pi\mathrm{c}/\lambda$ and vacuum speed of light c, in our case these are vectorial fields with electric part $\boldsymbol{E}$ and magnetic part $\boldsymbol{H}$, which can be written as $(\boldsymbol{E}, \boldsymbol{H})(x, y, z) = \boldsymbol{\Psi}(x, z)\exp(-\mathrm{i}\beta z)\exp(-\mathrm{i}k_y y)$. Here, k_y is the common wavenumber, as introduced before in Eq. (1), and $\beta = kN_\mathrm{B}$ and N_B are the propagation constant and effective index of the Bloch mode. Its profile function $\boldsymbol{\Psi}$ needs to be periodic in z with the period Λ of the grating.

The modes are governed by the frequency-domain Maxwell equations with the k_y-substitute, restricted to a unit cell interval $z \in [0, \Lambda]$, preferably chosen such that its boundary positions do not coincide with any dielectric interfaces (cf. Fig. 3). These vectorial equations are then solved for homogeneous, phase-adjusted periodic boundary conditions $(\boldsymbol{E}, \boldsymbol{H})(x, y, \Lambda) = (\boldsymbol{E}, \boldsymbol{H})(x, y, 0)\exp(-\mathrm{i}\beta\Lambda)$ and $\partial_z(\boldsymbol{E}, \boldsymbol{H})(x, y, \Lambda) =$

$\partial_z(\boldsymbol{E},\boldsymbol{H})(x,y,0)\exp(-\mathrm{i}\beta\Lambda)$, with the range of wavenumbers restricted to the first Brillouin zone, such that $\beta \in [-\pi/\Lambda, \pi/\Lambda]$ or $N_\mathrm{B} \in [-\lambda/(2\Lambda), \lambda/(2\Lambda)]$.

Our technical procedure can be outlined as follows. We invoke the BEP solver on the unit cell domain. For given wavelength, the solver establishes a relation in the form $\mathsf{A}\boldsymbol{v} = \mathsf{B}\boldsymbol{v}'$ where matrices A, B connect vectors of amplitudes $\boldsymbol{v}$, $\boldsymbol{v}'$ that represent the electromagnetic field at the beginning and the end of the unit cell. The former boundary conditions then require that $\boldsymbol{v}' = \exp(-\mathrm{i}\beta\Lambda)\boldsymbol{v}$ holds. Valid modes can thus be calculated as pairs of solutions $(\boldsymbol{v}, b)$ of the generalized eigenvalue problem $\mathsf{A}\boldsymbol{v} = b\mathsf{B}\boldsymbol{v}$. Among the set of results, complex eigenvalues b with $|b| = 1$ lead to the propagation constants $\beta = \pm(\arg b)/\Lambda$ and effective indices $N_\mathrm{B} = \beta/k$ of guided Bloch modes; the related eigenvectors represent the (fully vectorial, hybrid) mode profiles. The modes come in pairs of forward- and backward traveling fields.

Note that, due to the negative effective permittivity associated with the background medium, the concept of a light line [67] does not apply in the present case. Lossless guided Bloch modes with small effective indices exist even in the short-wavelenth regime.

2.3 Excitation by semi-guided beams of limited width

Obviously, in a practically relevant setting of integrated optics, all propagating waves need to be of limited lateral extension. Following the recipes of Refs. [28, 29, 35, 44, 49], this can be modeled by superimposing the former semi-guided plane waves with suitable weights over some range of wavenumbers k_y, or range of propagation angles, respectively. One forms bundles of semi-guided waves, or semi-guided "beams". Besides Gaussian superpositions [28, 35, 44, 49], also bundles generated from rib waveguides with shallow etching [29] have been studied.

For our gratings we consider TE-polarized bundles with Gaussian weight distribution, such that the resulting fields are vertically (x-) guided and in-plane (y, z) of Gaussian shape. The beams are focused at the origin $(y, z) = (0, 0)$ and are characterized by a principal angle of incidence θ and a beam width W_b (full width of the field at focus, in the direction perpendicular to the principal direction of propagation, $1/\mathrm{e}$-level). Our simulations rely on numerical integration of the BEP solutions of Section 2.1, according to explicit expressions from Refs. [28, 44].

3 A symmetric high contrast grating

Fig. 3 introduces our first example. Parameters as given for Fig. 2 apply: A series of N rectangular parallel grooves of width g with period Λ are etched into a slab waveguide of thickness $d = 220\,\mathrm{nm}$. The core with refractive index $n_\mathrm{g} = 3.45$ is embedded in a background medium with index $n_\mathrm{b} = 1.45$. Oblique incidence, according to Fig. 1, of TE-polarized semi-guided waves at an angle $\theta = 45°$ is considered, for some spectral range around the target vacuum wavelength $\lambda = 1.55\,\mu\mathrm{m}$.

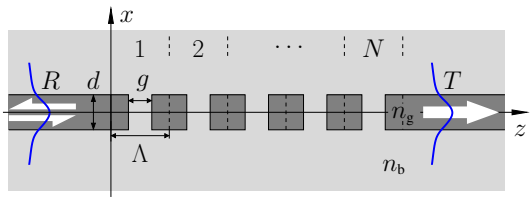

Figure 3: A finite fully-etched high-contrast grating in a slab waveguide, cross-sectional view. The interior grating region consists of N periods of length Λ, with central grooves of width g. The grating connects to exterior half-infinite slab waveguides of thickness d, made of media with refractive indices n_g (guiding regions) and n_b (background).

We first look at the strictly periodic interior segment of the grating, in terms of band structure calculations as outlined in Section 2.2. Fig. 4 compares band diagrams for gratings with different periods and gap widths. Effective indices for hybrid guided Bloch modes of dominant TE and TM polarization are shown. No limitation by any "light-line" applies (or the light-line is reduced to the $N_\mathrm{B} = 0$ -axis); lossless guided Bloch modes with down to zero effective indices are supported also at the short wavelength, or high frequency, end of the spectral region shown in the figure.

Two TE bandgap intervals appear, where no guided TE polarized Bloch modes are supported. For these wavelengths a segment of grating, with the respective periodicity and gap width, will act as a reflector, with a reflectance that grows with the number of periods. In some instances, guided TM Bloch modes are supported

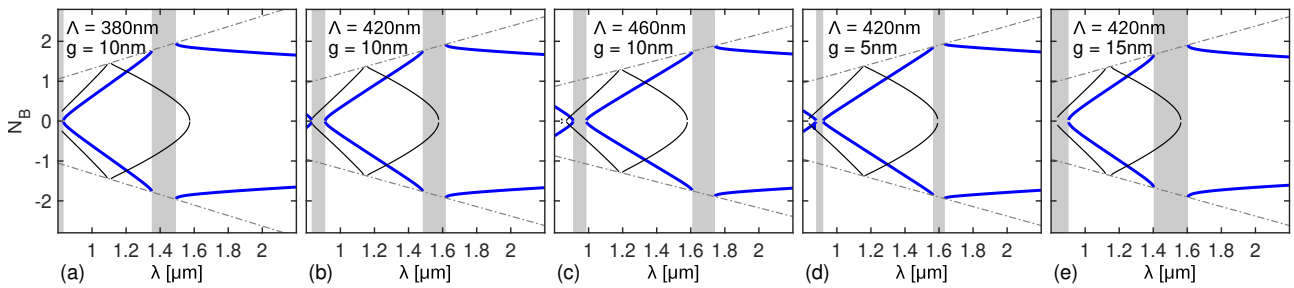

Figure 4: Band diagrams for infinite periodic gratings as in Fig. 3, for TE excitation at angle $\theta = 45°$, effective indices N_B of TE- (thick lines, blue) and TM-polarized Bloch modes (thinner curves, black), as a function of the excitation wavelength λ, and for values of period Λ and gap width g as given in the panels. Thin dash-dotted lines mark the borders of the first Brillouin zone at $\pm\lambda/(2\Lambda)$. Gray patches indicate the bandgaps for TE polarized Bloch modes.

at frequencies inside the TE band gaps. These, however are of a different symmetry class as any TE wave incident on a finite grating, and thus do not contribute to any transmission across the grating; the TE bandgap is symmetry protected.

What concerns the position and the widths of the bandgaps, one observes the following trends. A change in the period Λ of the grating, for constant gap g, mainly leads to a change in the position of the bandgaps (compare parts (a), (b), and (c) of Fig. 4). Contrary, an increase in the width g of the gaps causes an increase in the reflector strength associated with individual grooves, and thus mainly an increase in the width of the bandgaps (compare insets (d), (b), and (e)), with some minor change in the bandgap positions.

Next, we specialize to a grating with the parameters $\Lambda = 420\,\text{nm}$, $g = 10\,\text{nm}$. Fig. 4(b) predicts a major TE-bandgap (wider gray patch) of width $136\,\text{nm}$, extending from $1.483\,\mu\text{m}$ to $1.619\,\mu\text{m}$, roughly centered at our target wavelength $1.55\,\mu\text{m}$. Fig. 5 shows respective transmittance and reflectance spectra, for a series of finite gratings.

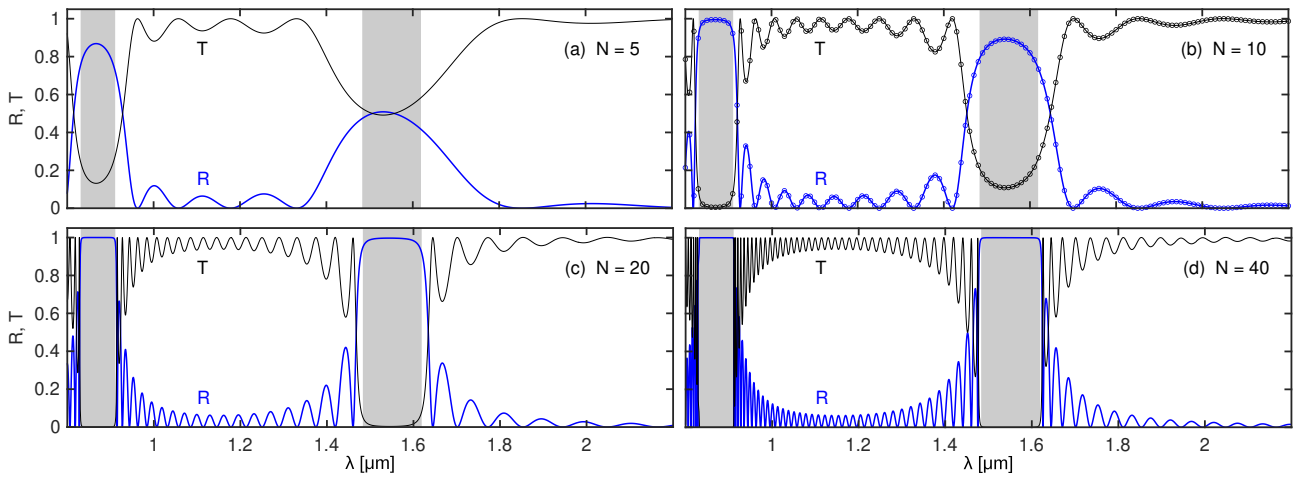

Figure 5: Reflectance R and transmittance T versus vacuum wavelength λ, for finite gratings as in Fig. 3 with $N = 5, 10, 20, 40$ periods (a–d), period length $\Lambda = 420\,\text{nm}$, and gap width $g = 10\,\text{nm}$, for TE excitation at angle $\theta = 45°$. Gray patches show the bandgap regions as identified in Fig. 4(b). Panel (b), markers: FE simulations, cf. Section 2.1.1.

As expected, the bandgaps appear as wavelength regions with high reflectance R and accordingly low transmittance T. In line with Section 2, $R + T = 1$ holds strictly for the present configurations. For increasing number of inner periods, the reflectance maxima attain a shape with more and more flattened top. A pronounced slope in the reflectance curves in the bandgap regions, as associated with radiation losses in other settings [7], is entirely absent in the present configurations.

The spectral regions between the bandgaps are filled with a series of resonance peaks, with extremal states of full transmittance and zero reflectance. These can be understood as transmission resonances of guided Bloch modes between the two interfaces that separate corrugated and non-corrugated slab regions. With more inner periods, the then longer interior grating supports more and more of these resonances. Also here one obtains clear spectral features that are not obscured by any radiation losses.

Fig. 6 collects a few field impressions, for configurations with maximum reflectance at the target wavelength,

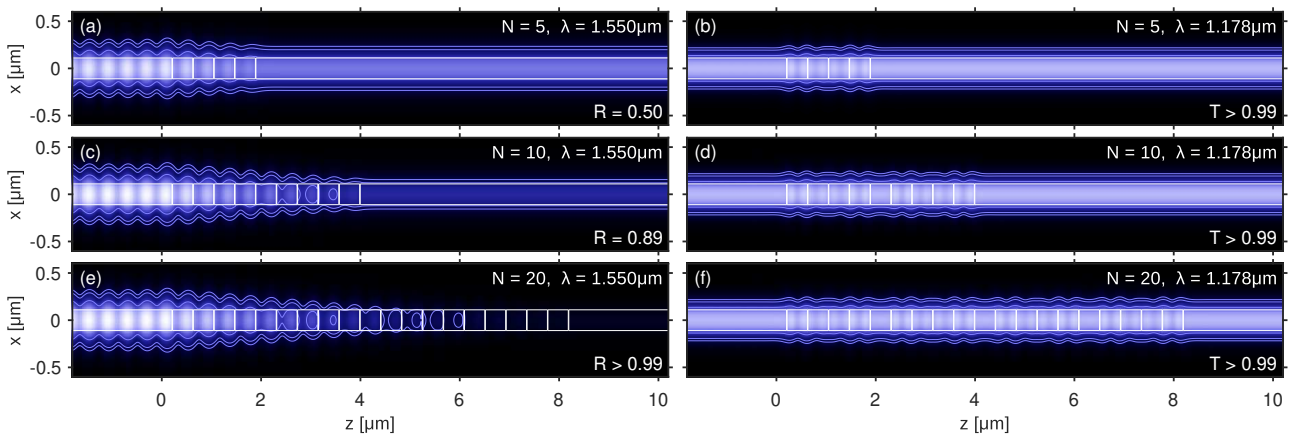

Figure 6: Excitation of gratings with parameters as in Fig. 5, $\Lambda = 420$ nm, $g = 10$ nm, with numbers of periods $N = 5$ (a, b), $N = 10$ (c, d), $N = 20$ (e, f), by semi-guided TE polarized plane waves at angle $\theta = 45°$, at wavelengths $\lambda = 1.55\,\mu$m, (a, c, d) and $\lambda = 1.178\,\mu$m (b, d, f); optical electromagnetic energy density u on the x-z-cross section plane; contour lines at 5%, 1%, and 0.5% of the maximum level, with a uniform color scale for all panels.

and for configurations with full transmittance at the central maximum between the two bandgap regions. These are vectorial fields where various components play a role. We thus plot the time-averaged energy density $u = \mathrm{Re}\,(\epsilon_0 n^2|\boldsymbol{E}|^2 + \mu_0|\boldsymbol{H}|^2)/4$ of the frequency domain optical field with electric part $\boldsymbol{E}$, magnetic part $\boldsymbol{H}$, and vacuum permittivity ϵ_0 and permeability μ_0. At the wavelength inside the bandgap (parts (a), (c), (e)), one observes gradually decaying field levels in the corrugated regions. Longer gratings thus effect an increasing reflectance. At the particular wavelength outside the bandgap (panels (b), (d), (f)), the interference of forward- and backward traveling Bloch modes leads to an irregular field pattern in the corrugated region that repeats itself for a growing number of periods, establishing the (weak) transmission resonance. All fields are clearly vertically confined around the slab core.

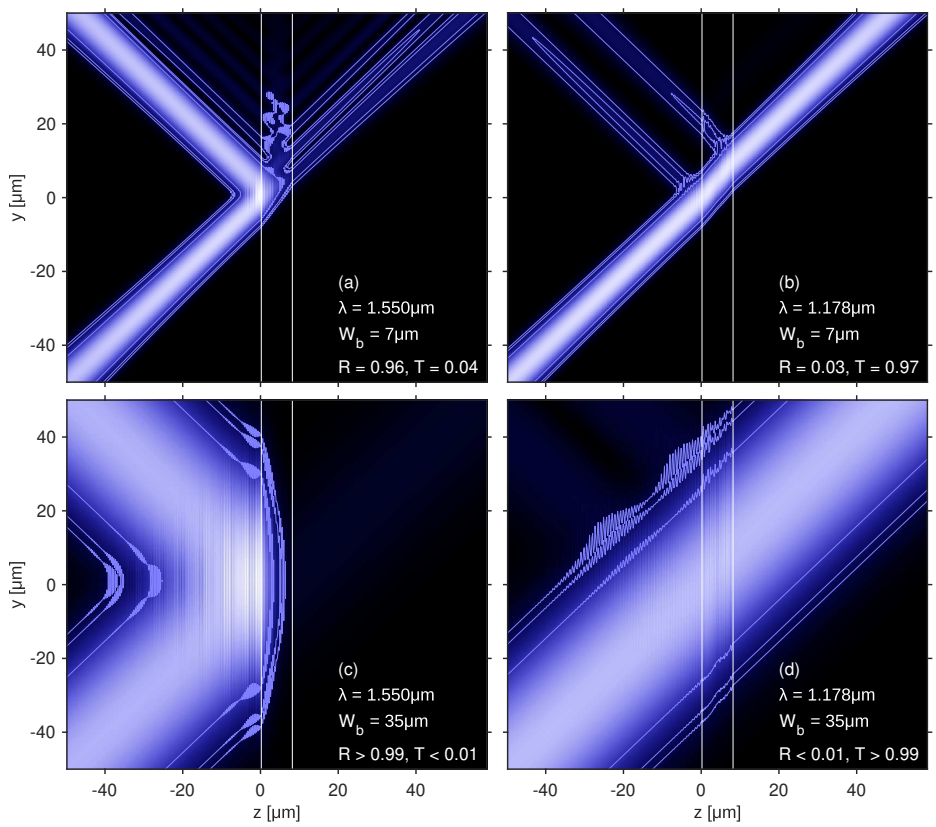

Figure 7: Excitation of gratings as in Fig. 3 by bundles of semi-guided waves; energy density u on the y-z-plane at the core center $x = 0$; contour lines at 5%, 1%, and 0.5% of the maximum level, with a uniform color scale for all panels. Parameters are as for Fig. 5, $\Lambda = 420$ nm, $g = 10$ nm, a grating with $N = 20$ periods; oblique incidence of beams of cross-sectional widths $W_b = 7\,\mu$m (a, b) and $W_b = 35\,\mu$m (c, d) at wavelengths $\lambda = 1.55\,\mu$m, (a, c) and $\lambda = 1.178\,\mu$m (b, d). Values of reflectance R and transmittance T are shown. White lines indicate only the outermost interfaces of the corrugated region.

As a further illustration, we consider a "top view" of the propagation across the gratings, now for wave bundles of limited width, as discussed in Section 2.3. Fig. 7 collects respective plots, for incidence of narrower and wider beams at the two wavelengths of Fig. 6. By construction, the bundles cover plane waves for a range of wave vectors, or range of angles of incidence, respectively, centered around a principal angle θ. As the plane wave transmission properties vary with incidence angle, the transmittance and reflectance observed for bundled incidence differs from the values as predicted for plane wave incidence at the principal angle. Accordingly, for the narrower beams in Fig. 7(a, b) one observes some residual transmission, or reflection, respectively. For the spatially wider beams in panels (c, d) with their narrower range of relevant wavenumbers, we find again transmittance and reflectance values close to the levels for plane wave excitation.

3.1 Apodized grating

The pronounced ripples in the spectra of the former gratings in the wavelength regions outside the bandgaps can be understood as resonances of the Bloch modes between the two interfaces of the periodically corrugated inner grating region and the external non-corrugated slabs. Tapering these transitions can be expected to lower the reflectance associated with the interfaces, and thus to reduce the transmittance ripples. Various types of apodization have been applied widely [5, 68, 69] as a means to shift the spectrum with a more box-like, flatter shape closer to full transmittance and zero reflectance outside the bandgap regions.

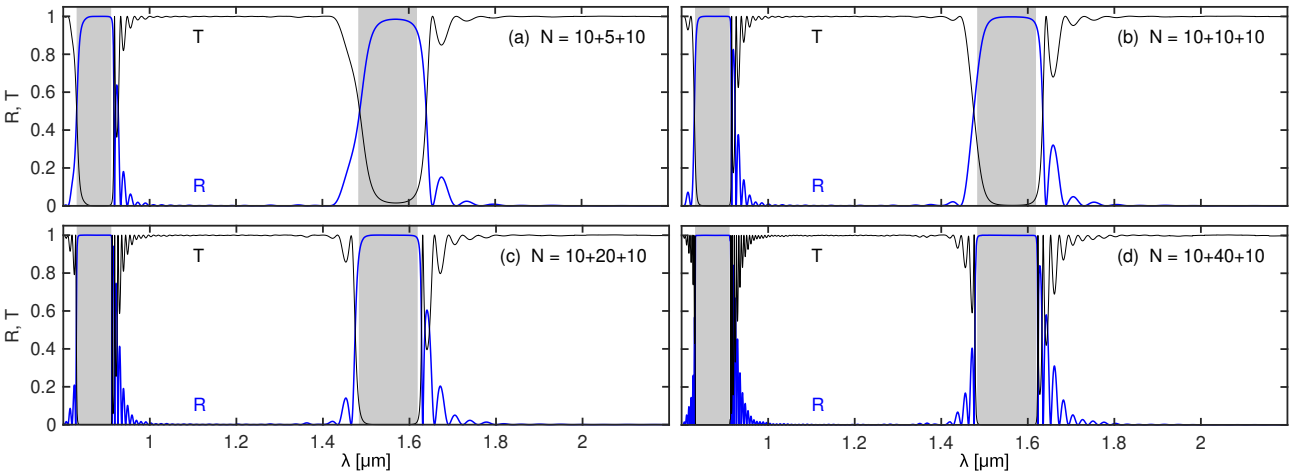

Figure 8: Reflectance R and transmittance T versus wavelength λ, for apodized gratings with parameters $\Lambda = 420$ nm, $g = 10$ nm, and a number of inner periods $5, 10, 20, 40$ (a–d), continued on both sides by 10 periods with gap widths that decrease linearly outwards down to a minimum width of 2 nm. Gray patches: bandgap regions as identified in Fig. 4(b) for the original, strictly periodic structures with 10 nm gap width.

For the spectra in Fig. 8 we tried a very simple type of linear apodization. The former gratings are surrounded by additional periods on both sides, where, starting with the first period outside the original range, the gap width g is reduced linearly outwards from the original values of 10 nm down to a minimum width of 2 nm for the outermost periods, for constant period length Λ. Comparison with the spectra in Fig. 5 clearly shows the expected effects, where there is certainly room for further optimization of the shape and length of the apodization.

4 Grating with reduced reflector strength

A more narrowband reflection spectrum could be seen as potential aim for our gratings. According to the discussion of the band diagrams around Fig. 4, that should be attainable by reducing the gap width of the former fully-etched devices. Unfortunately, this would quickly lead to rather unrealistic trenches of few- or sub-nanometer width. As an alternative, one can reduce the reflector strength of the individual grooves, by only partly removing the waveguide core in the groove regions. The structure of Fig. 9 maintains the $\pm x$-symmetry, such that polarization conversion is still prohibited.

We focus on only one groove first. Fig. 10 shows the reflectance associated with a single grating period, for varying residual core thickness in the gaps of the grating. For the fully etched grating with $r = 0$, with growing

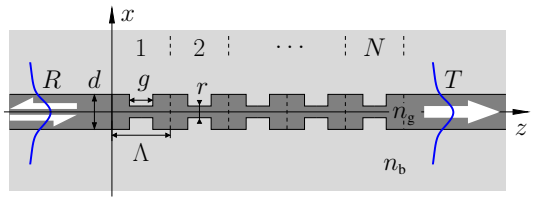

Figure 9: Cross-section of a finite partly-etched symmetric high-contrast grating. Parameters are as introduced in Fig. 3, with a residual film thickness r in the groove regions.

groove width g the reflectance rises steeply towards total reflectance. This can be understood as an effect of frustrated total internal reflection [70], here for the purely evanescent fields that "reach out" from the input slab across the gap to the output slab segment [55]. The same mechanism can apply in a structure with a residual core that supports guided modes: At small r, these modes have sufficiently low effective indices, such that the critical angle (4) of these modes, for TE-excitation by the fundamental mode of the original slab, is below the $45°$ angle of incidence as assumed for these calculations. Hence, even if guided modes are supported by the thin slab profile associated with the groove regions, these modes become evanescent for the present oblique excitation. For larger $r > 79.5$ nm, however, the critical angle is above the $45°$-level, such that the modes can propagate within the gap region. Then the two groove interfaces act as two identical (weak) reflectors of a resonant system. In that case of large r, wide transmission resonances can be observed, periodic in g.

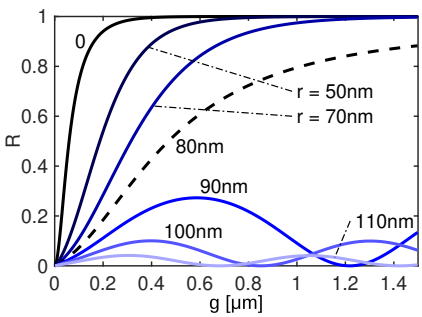

Figure 10: Reflectance R of single grooves of width g (see Fig. 9, $N = 1$) in a slab of thickness $d = 220$ nm for a residual core thickness r. Semi-guided TE excitation at wavelength $\lambda = 1.55\,\mu$m, at an angle $\theta = 45°$.

According to Fig. 10, the fully-etched grating ($r = 0$) of Fig. 5 with a gap width of 10 nm corresponds to a single-groove reflectance of about 0.03. Hence, spectra as in Fig. 5, with a similar magnitude of the bandgap, should be realizable alternatively with partly etched grooves for e.g. $r = 110$ nm and a larger gap $g = 170$ nm (and modified period length).

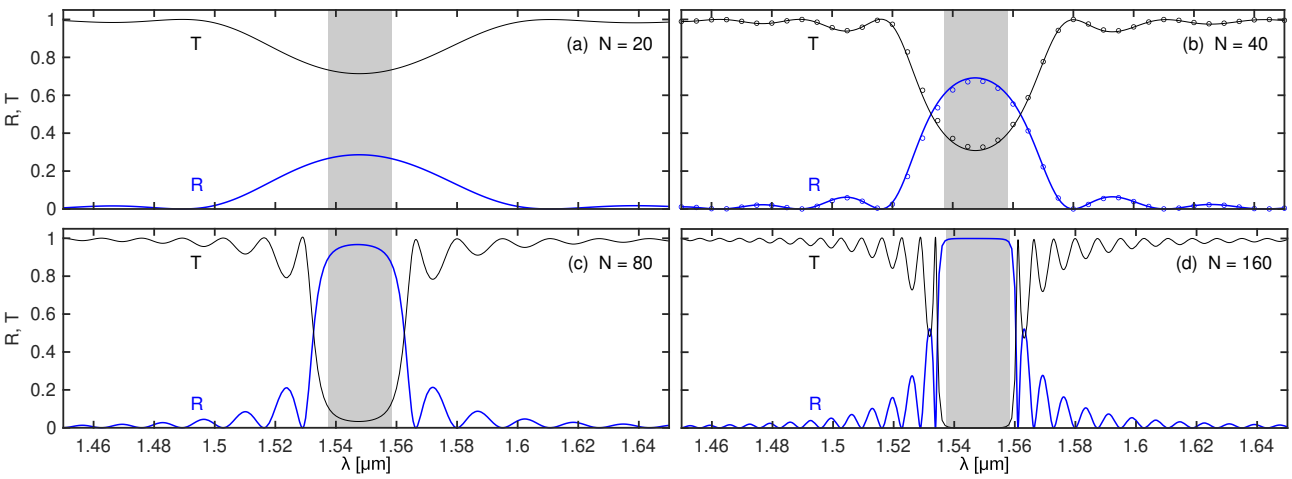

Figure 11: Reflectance R and transmittance T as a function of wavelength λ, for finite gratings as in Fig. 9 with $N = 20, 40, 80, 160$ periods (a–d) and period length $\Lambda = 411$ nm, gap width $g = 110$ nm, and remaining film thickness $r = 160$ nm in the groove regions. Gray patches mark the bandgap regions for the respective infinite periodic gratings, for oblique TE polarized excitation at $45°$. Note the wavelength range of only 200 nm. Markers in part (b) show the results of FE simulations (see Section 2.1.1).

Aiming at a grating with narrower-band reflectance, one needs to further reduce the reflector strength of the individual grooves. A band structure analysis procedure as before (not shown) predicts, for residual film thickness $r = 160$ nm, and gap with of $g = 110$ nm, a bandgap of roughly 20 nm (compare to the 136 nm of Fig. 5), as before centered close to our target wavelength of $\lambda = 1.55\,\mu$m. The respective spectra in Fig. 11 are of similar form as those for the fully etched gratings, but concern a much shorter wavelength interval. The gratings realize

the narrower bandgap with a similar period length and with perhaps a little more convenient groove width. This, however, comes at a prize of substantially more periods, i.e. of longer gratings, that are required for a spectral response with a flat-top reflection band. Apodization should be possible just as described in Section 3.1.

5 Narrow-band Fabry-Perot filter

A standard technique for creating narrow-band transmission filters is to introduce a suitable defect into an otherwise periodic grating [67,71,72]. If operated at wavelengths inside its bandgap region, the grating without the defect, or the two halves enclosing the defect region, would act as a good reflectors. That procedure could certainly also be pursued with the present grating configurations (not followed up here).

Alternatively, according to Fig. 10, lossless reflectors of quite arbitrary (large) strength for semi-guided waves can be created by just using a *single wide trench* [55]. These rely on frustrated total internal reflection only, not on any resonant effect. Therefore, while moderately wavelength dependent, the reflectance of these trenches is reasonably broadband [55]. We are thus led to the structure shown in Fig. 12.

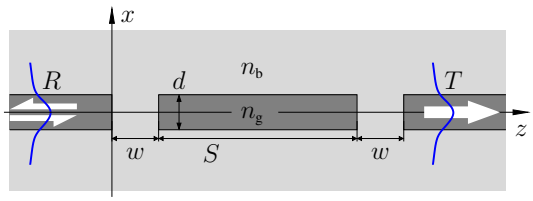

Figure 12: Filter of Fabry-Perot type, to be excited by semi-guided waves at oblique angles. A slab waveguide of thickness d, with refractive indices n_g (core) and n_b (background) includes two identical trenches of width w that are separated by a distance S.

The device constitutes an instance of what has been proposed as a two-groove planar filter (TGPF) in Ref. [34], there discussed in terms of the leaky modes supported by the (narrow) central slab region, for non-symmetric structures with wider, only partly-etched trenches. As an alternative, the filters can also be understood by common arguments for Fabry-Perot resonators [55]. We shall see that widened (highly "multimode") central regions can lead to sharpened resonances, and we shall look at the bundled excitation of these devices.

Apart from the properties of the slab waveguide (values as before), the filter geometry and thus its transmission characteristics are determined by the width w of and the distance S between the two trenches. Of these, the gap w controls the reflectance associated with each individual trench. Rather arbitrarily, we look at widths of $w \in [100, 200, 300]$ nm, leading to single trench reflectances of $R = 0.74$, 0.94, and 0.98, according to Fig. 10. Aiming at full transmission at our target wavelength of $\lambda = 1.55\,\mu$m, we then vary S to identify values where the double-trench resonator supports a transmission resonance at this wavelength (curves not shown).

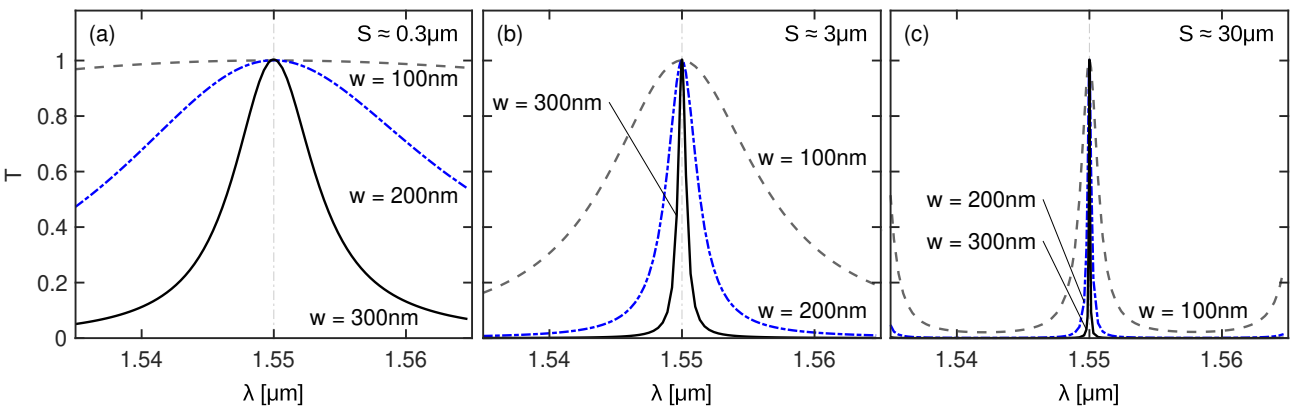

Figure 13: Transmittance T versus vacuum wavelength λ, for double-trench resonators as in Fig. 12, for trench widths $w = 100$ nm (dash-dotted), $w = 200$ nm (dashed), $w = 300$ nm (solid curve), and reflector separations S close to $0.3\,\mu$m (a), $3\,\mu$m (b), and $30\,\mu$m (c), respectively.

Standard Fabry-Perot theory [73] can be applied. For fixed reflector strength, and at given wavelength, the transmission resonances appear periodically in the reflector distance S, in our case spaced by $\Delta S = \lambda/(2N_{\rm TE}\cos\theta)$, where $N_{\rm TE}\cos\theta$ is the effective index relevant for the the propagation of the fundamental TE wave along z, for excitation at angle θ. One obtains a distance $\Delta S = 0.388\,\mu$m for our present parameters. Having selected, for each w, a suitable value S_0 close to $0.3\,\mu$m, we are led to configurations with $w = 100$ nm, $S \in [0.314, 3.418, 30.210]\,\mu$m, alternatively $w = 200$ nm, $S \in [0.335, 3.439, 30.231]\,\mu$m, and $w = 300$ nm,

$S \in [0.340, 3.444, 30.236]\,\mu$m that show transmittance maxima at $\lambda = 1.55\,\mu$m. Each set of values for the trench distance constitutes a triple $[S_0,\, S_0 + 8\Delta S,\, S_0 + 77\Delta S]$. Fig. 13 compares the corresponding spectra.

For separations S of similar magnitude, the spectral width of the transmission resonances decreases with growing reflector strength, i.e. with growing width w. Likewise, the transmission peaks become sharper for increasing resonator length S. This can again be understood by standard expressions from Fabry-Perot theory. These predict a free spectral range, a wavelength distance between neighboring transmission resonances, of $\Delta\lambda = \lambda^2/(2Sn_\mathrm{g})$ and a spectral width (full width at half maximum) of the transmittance peaks of $2\delta\lambda = (\lambda^2\phi_{1/2})/(2\pi S n_\mathrm{g})$. Here $\phi_{1/2}$ is some phase factor (w-dependent), and n_g is the group index $n_\mathrm{g} = (N_\mathrm{TE} - \lambda\partial_\lambda N_\mathrm{TE})\cos\theta$ relevant for the propagation of the oblique TE-wave along z at angle θ. Both the free spectral range as well as the peak width scale inversely with the reflector separation S.

The larger resonators in Fig. 13(b, c) are characterized by spectral widths of about $2\delta\lambda = 13.6$ nm, 2.7 nm, 0.7 nm for $w = 100$, 200, 300 nm, and $S \approx 3\,\mu$m (b), and of $2\delta\lambda = 1.51$ nm, 0.3 nm, 0.08 nm for $w = 100$, 200, 300 nm, and $S \approx 30\,\mu$m (c). This confirms the $1/S$-dependence of the spectral peak width, which in part (c) of Fig. 13 is roughly $1/10$ of the width seen in the configuration with the same trench width w in (b). What concerns the free spectral range, for the configurations of Fig. 13(c) one finds a value $\Delta\lambda = 15.7$ nm (neighboring peaks not shown). This agrees well with a predicted value of $\Delta\lambda = 15.9$ nm, for a group index $n_\mathrm{g} = 2.51$ estimated with the data in Fig. 2. One can associate Q-factors $Q = \lambda/(2\delta\lambda)$ of $1.1 \cdot 10^2$, $5.7 \cdot 10^2$, $2.2 \cdot 10^3$ (b) and of $1.0 \cdot 10^3$, $5.2 \cdot 10^3$, $1.9 \cdot 10^4$ (c) with these resonators.

We wrap up this discussion with impressions of the associated optical fields, for the intermediate configuration of Fig. 13(b) for $w = 200$ nm. Fig. 14 shows field profiles on the cross-sectional x-z plane, for oblique incidence of lateral plane waves, for excitation at the transmission resonance, and off-resonance. The fields differ in particular with respect to the field levels seen in the region between the reflectors. At resonance (b), the maximum value of the energy density is by a factor 16 larger than at the off-resonance wavelength (a).

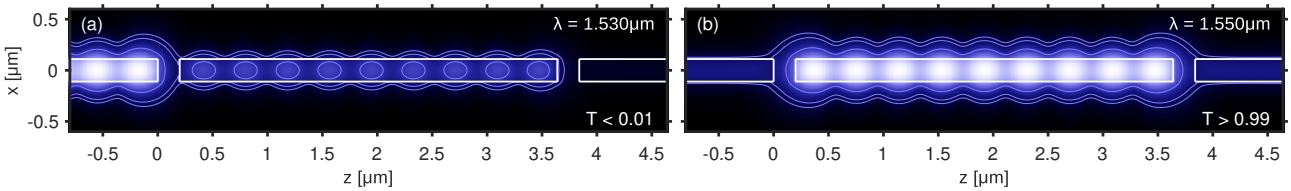

Figure 14: Oblique excitation of the double-trench resonator with $w = 200$ nm, $S = 3.439\,\mu$m by semi-guided plane waves at vacuum wavelength $\lambda = 1.53\,\mu$m (a), and $\lambda = 1.55\,\mu$m (b). Values of transmittance T and reflectance R are shown. Color levels in (a) and (b) are not comparable; contour lines are shown for 5%, 1%, and 0.5% of the maximum levels, separately for both panels.

Just as for the excitation wavelength, these resonators must be suspected to be extremely sensitive to all other model parameters, including the angle of incidence. Fig. 15 compares results if the former structure is excited by semi-guided wave bundles of varying width W_b, where a range of angles of incidence around the principal angle $\theta = 45°$ contribute. Note the axis units of millimeters; on this scale, the tiny ripples of the field, caused by the presence of partly counterpropagating waves, are not fully resolved; also the interfaces associated with the resonator cannot be distinguished.

In case of the off-resonance excitation in panels (a), (b), and (c), with full reflection for all beam widths that were considered, the structure works as predicted for plane wave excitation. This is different at the resonant wavelength, where the transmission properties for bundled excitation come close to the values for plane wave input, if the beam width is sufficiently large. Apparently, for narrower beams with a correspondingly wider range of wavenumbers k_y that contribute with relevant amplitudes, only part of that distribution is "caught" by the narrow resonance peak. Still, even for the smallest beams considered here, with $W_\mathrm{b} = 100\,\mu$m, the resonator singles out about 39% of the power at the resonance wavelength. That transmittance raises to a level of 0.999, if the bundle width W is increased to 5 mm (field not shown, we tried only a few larger beam widths).

On the scale of the figures and for the present wide wave bundles, hardly any noticeable shift upon reflection along y can be observed for the beams off-resonance (Goos-Hänchen-shift [22,56,74]). For resonant excitation, panels (d), (e), and (f) show a substantial shift of the center of the transmitted beams along y. This points at a mechanism where a field confined to the central part of the resonator is excited, that, after propagating a distance along y, gradually leaks away [44].

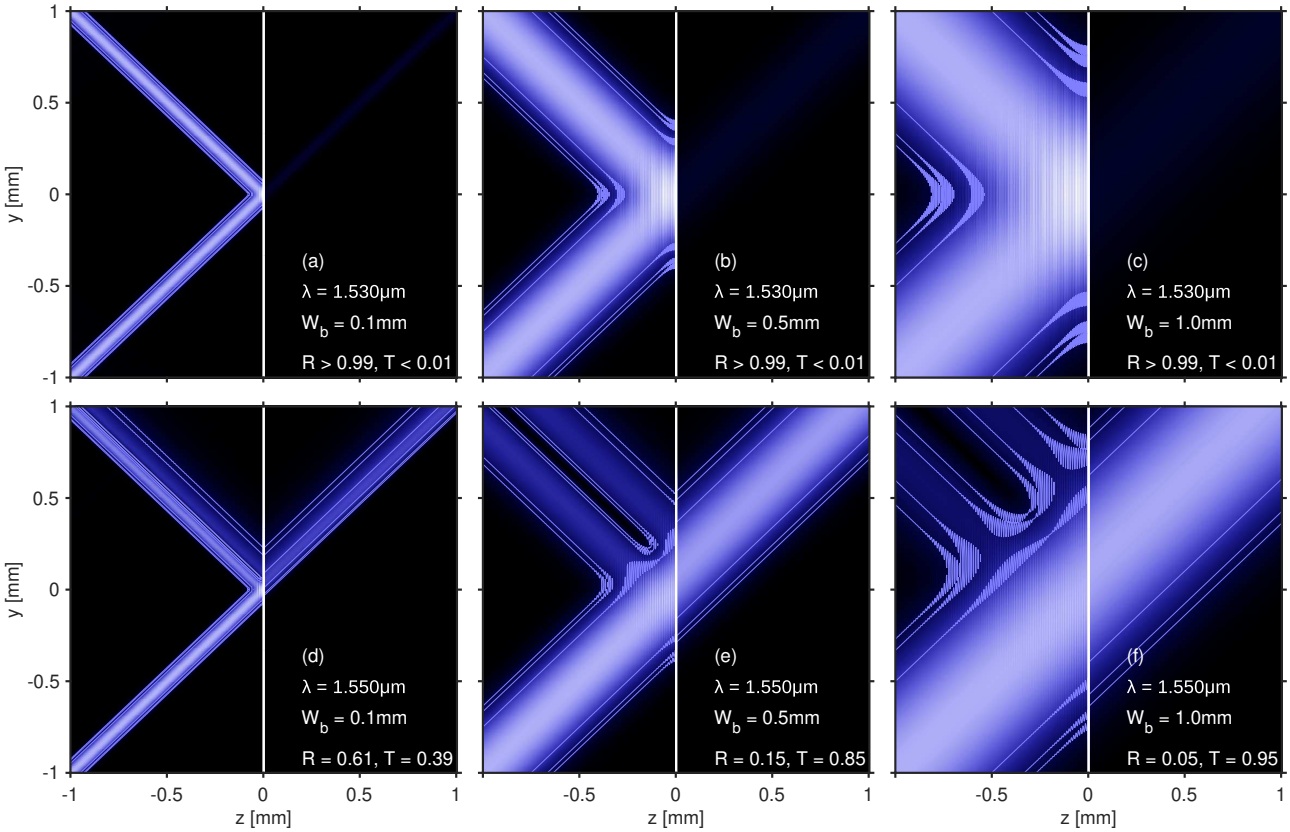

Figure 15: Excitation of the resonators of Fig. 12, with $w = 200$ nm, $S = 3.439\,\mu$m, by TE polarized semi-guided beams of width W_b, at a principal angle of $45°$, at wavelengths of $\lambda = 1.530\,\mu$m (a, b, c) and $\lambda = 1.550\,\mu$m; energy density u in the y-z-plane at the core center $x = 0$. Color scales of plots for the same W_b (e.g. (a) and (d)) are comparable; contour lines indicate 5%, 1%, and 0.5% of the maximum levels. Values for transmittance T and reflectance R are given.

6 Concluding remarks

Symmetric, fully- and partly etched finite high-contrast waveguide Bragg gratings with 1-D periodicity have been investigated, as well as a narrow-band Fabry-Perot filter, for oblique excitation by semi-guided waves at $45°$ angle of incidence, with typical parameters from silicon photonics. Assuming, for the present theoretical models, lossless media and perfect interfaces, the gratings do not show any radiative losses. Also, polarization and mode conversion are prohibited. We have discussed configurations with reflection bands or transmittance peaks of widths 136 nm (Sections 3, 3.1), 20 nm (Section 4) down to $[13.6, 0.08]$ nm (Section 5). The grating-based devices can act as wavelength filters with reasonably flat-top response; apodization can lead to even more box-shaped spectra.

Clearly, just as the other proposals mentioned in the introduction, the present gratings are not directly compatible with the "photonic wires" of silicon photonics. Rather, one envisions photonic circuits that are based entirely on semi-guided waves, then combining our gratings with any of the former components. Connections to the standard single mode channel waveguides, where necessary, could be realized by suitable tapers [32], or specific grating couplers ("Bragg deflectors") [75]. Direct end-facet coupling with suitable (cylindrical) lenses, or gratings for fiber-to-chip coupling [9–12], adapted to the wide semi-guided field, could serve for out-of-chip connections.

Due to the absence of radiative losses, and the restriction to single mode operation (externally, but partly also internally, for spatial intervals beyond the range of the "other" evanescent waves), the devices are akin to conventional dielectric multilayer structures with 1-D periodicity [67]. Consequently, all sophisticated optimization and design techniques established in that field could be applied, in principle (see e.g. [76]), for further tailoring the spectral properties of the present gratings.

Funding

Financial support from the German Research Foundation (Deutsche Forschungsgemeinschaft DFG, project 231447078–TRR 142, subproject B06) is gratefully acknowledged.

Disclosures

The authors declare no conflicts of interest.

Data availability

Data underlying the results presented in this paper are not publicly available at this time but may be obtained from the authors upon reasonable request.

References

[1] J.-W. Mu, H. Zhang, and W.-P. Huang. Design of waveguide Bragg gratings with strong index corrugations. *Journal of Lightwave Technology*, 26(12):1596–1601, 2008.

[2] R.. Halir, P. J. Bock, P. Cheben, A. Ortega-Moñux, C. Alonso-Ramos, J. H. Schmid, J. Lapointe, D.-X. Xu, J. G. Wangüemert-Pérez, Í. Molina-Fernández, and S. Janz. Waveguide sub-wavelength structures: a review of principles and applications. *Laser & Photonics Reviews*, 9(1):25–49, 2015.

[3] P. Cheben, R. Halir, J. H. Schmid, H. A. Atwater, and D. R. Smith. Subwavelength integrated photonics. *Nature*, 560:565–572, 2018.

[4] S. Kaushal, R. Cheng, M. Ma, A. Mistry, M. Burla, L. Chrostowski, and J. Azaña. Optical signal processing based on silicon photonics waveguide Bragg gratings: review. *Frontiers of Optoelectronics*, 11:163–188, 2018.

[5] R. Cheng and L. Chrostowski. Spectral design of silicon integrated Bragg gratings: A tutorial. *Journal of Lightwave Technology*, 39(3):712–729, 2021.

[6] M. Palamaru and P. Lalanne. Photonic crystal waveguides: Out-of-plane losses and adiabatic modal conversion. *Applied Physics Letters*, 78(11):1466–1468, 2001.

[7] J. Čtyroký, S. Helfert, R. Pregla, P. Bienstman, R. Baets, R. de Ridder, R. Stoffer, G. Klaase, J. Petráček, P. Lalanne, J.-P. Hugonin, and R. M. De La Rue. Bragg waveguide grating as a 1D photonic band gap structure: Cost 268 modelling task. *Optical and Quantum Electronics*, 34(5/6):455–470, 2002.

[8] M. Hammer. Quadridirectional eigenmode expansion scheme for 2-D modeling of wave propagation in integrated optics. *Optics Communications*, 235(4–6):285–303, 2004.

[9] M. L. Dakss, L. Kuhn, P. F. Heidrich, and B. A. Scott. Grating coupler for efficient excitation of optical guided waves in thin films. *Applied Physics Letters*, 16(12):523–525, 1970.

[10] D. Taillaert, P. Bienstman, and R. Baets. Compact efficient broadband grating coupler for silicon-on-insulator waveguides. *Optics Letters*, 29(23):2749–2751, 2004.

[11] C. Alonso-Ramos, A. Ortega-Moñux, L. Zavargo-Peche, R. Halir, J. de Oliva-Rubio, I. Molina-Fernández, P. Cheben, D.-X. Xu, S. Janz, N. Kim, and B. Lamontagne. Single-etch grating coupler for micrometric silicon rib waveguides. *Optics Letters*, 36(14):2647–2649, 2011.

[12] L. Cheng, S. Mao, Z. Li, Y. Han, and H. Y. Fu. Grating couplers on silicon photonics: Design principles, emerging trends and practical issues. *Micromachines*, 11(7):666, 2020.

[13] A. David, H. Benisty, and C. Weisbuch. Photonic crystal light-emitting sources. *Reports on Progress in Physics*, 75(12):126501, 2012.

[14] W.-L. Yeh, C.-M. Fang, and Y.-P. Chiou. Enhancing LED light extraction by optimizing cavity and waveguide modes in grating structures. *Journal of Display Technology*, 9(5):359–364, 2013.

[15] K.O. Hill and G. Meltz. Fiber Bragg grating technology fundamentals and overview. *Journal of Lightwave Technology*, 15(8):1263–1276, 1997.

[16] W. C. L. Hopman, P. Pottier, D. Yudistira, J. van Lith, P. V. Lambeck, R. M. De La Rue, A. Driessen, H. J. W. M. Hoekstra, and R. M. de Ridder. Quasi-one-dimensional photonic crystal as a compact building-block for refractometric optical sensors. *IEEE Journal of Selected Topics in Quantum Electronics*, 11(1):11–16, 2005.

[17] N. N. Klimov, S. Mittal, M. Berger, and Z. Ahmed. On-chip silicon waveguide Bragg grating photonic temperature sensor. *Optics Letters*, 40(17):3934–3936, 2015.

[18] M. A. Butt, N. L. Kazanskiy, and S. N. Khonina. Advances in waveguide Bragg grating structures, platforms, and applications: An up-to-date appraisal. *Biosensors*, 12(7), 2022.

[19] S. Wang. Principles of distributed feedback and distributed Bragg-reflector lasers. *IEEE Journal of Quantum Electronics*, 10(4):413–427, 1974.

[20] A. W. Fang, B. R. Koch, R. Jones, E. Lively, D. Liang, Y.-H. Kuo, and J. E. Bowers. A distributed Bragg reflector silicon evanescent laser. *IEEE Photonics Technology Letters*, 20(20):1667–1669, 2008.

[21] Y. Han, H. Park, J. Bowers, and K. M. Lau. Recent advances in light sources on silicon. *Advances in Optics and Photonics*, 14(3):404–454, Sep 2022.

[22] F. Çivitci, M. Hammer, and H. J. W. M. Hoekstra. Semi-guided plane wave reflection by thin-film transitions for angled incidence. *Optical and Quantum Electronics*, 46(3):477–490, 2014.

[23] M. Hammer, L. Ebers, A. Hildebrandt, S. Alhaddad, and J. Förstner. Oblique semi-guided waves: 2-D integrated photonics with negative effective permittivity. In *2018 IEEE 17th International Conference on Mathematical Methods in Electromagnetic Theory (MMET)*, pages 9–15, 2018.

[24] R. Ulrich and R. J. Martin. Geometrical optics in thin film light guides. *Applied Optics*, 10(9):2077–2085, 1971.

[25] P. K. Tien, S. Riva-Sanseverino, R. J. Martin, and G. Smolinsky. Two-layered construction of integrated optical circuits and formation of thin-film prisms, lenses, and reflectors. *Applied Physics Letters*, 24(11):547–549, 1974.

[26] P. K. Tien. Integrated optics and new wave phenomena in optical waveguides. *Reviews of Modern Physics*, 49(2):361–419, 1977.

[27] M. Hammer, A. Hildebrandt, and J. Förstner. How planar optical waves can be made to climb dielectric steps. *Optics Letters*, 40(16):3711–3714, 2015.

[28] M. Hammer, A. Hildebrandt, and J. Förstner. Full resonant transmission of semi-guided planar waves through slab waveguide steps at oblique incidence. *Journal of Lightwave Technology*, 34(3):997–1005, 2016.

[29] L. Ebers, M. Hammer, and J. Förstner. Oblique incidence of semi-guided planar waves on slab waveguide steps: Effects of rounded edges. *Optics Express*, 26(14):18621–18632, 2018.

[30] M. Hammer, L. Ebers, and J. Förstner. Oblique quasi-lossless excitation of a thin silicon slab waveguide: a guided-wave variant of an anti-reflection coating. *Journal of the Optical Society of America B*, 36(9):2395–2401, 2019.

[31] M. Hammer, L. Ebers, and J. Förstner. Optischer Übergang zwischen zwei optischen Schichtwellenleitern und Verfahren zum Übertragen von Licht. German Patent DE 10 2018 108 110 B3, Deutsches Patent- und Markenamt (filed 05.04.2018, issued 31.01.2019).

[32] W. P. Tresna, A. W. S. Putra, and T. Maruyama. Optical-loss measurement of a silicon-slab waveguide. *Current Optics and Photonics*, 4(6):551–557, 2020.

[33] E. A. Bezus, D. A. Bykov, and L. L. Doskolovich. Bound states in the continuum and high-Q resonances supported by a dielectric ridge on a slab waveguide. *Photonics Research*, 6(11):1084–1093, 2018.

[34] L. L. Doskolovich, E. A. Bezus, and D. A. Bykov. Two-groove narrowband transmission filter integrated into a slab waveguide. *Photonics Research*, 6(1):61–65, 2018.

[35] E. A. Bezus, L. L. Doskolovich, D. A. Bykov, and V. A. Soifer. Spatial integration and differentiation of optical beams in a slab waveguide by a dielectric ridge supporting high-Q resonances. *Optics Express*, 26(19):25156–25165, 2018.

[36] M. Hammer, L. Ebers, and J. Förstner. Oblique evanescent excitation of a dielectric strip: A model resonator with an open optical cavity of unlimited Q. *Optics Express*, 27(7):9313–9320, 2019.

[37] T. G. Nguyen, G. Ren, S. Schoenhardt, M. Knoerzer, A. Boes, and A. Mitchell. Ridge resonance in silicon photonics harnessing bound states in the continuum. *Laser & Photonics Reviews*, 13(10):1900035, 2019.

[38] T. G. Nguyen, K. Yego, G. Ren, A. Boes, and A Mitchell. Microwave engineering filter synthesis technique for coupled ridge resonator filters. *Optics Express*, 27(23):34370–34381, 2019.

[39] L. L. Doskolovich, E. A. Bezus, and D. A. Bykov. Integrated flat-top reflection filters operating near bound states in the continuum. *Photonics Research*, 7(11):1314–1322, 2019.

[40] D. A. Bykov, E. A. Bezus, and L. L. Doskolovich. Bound states in the continuum and strong phase resonances in integrated Gires-Tournois interferometer. *Nanophotonics*, 9(1):83–92, 2020.

[41] E. A. Bezus, D. A. Bykov, and L. L. Doskolovich. Integrated Gires–Tournois interferometers based on evanescently coupled ridge resonators. *Optics Letters*, 45(18):5065–5068, 2020.

[42] S. Schoenhardt, A. Boes, T. G. Nguyen, and A. Mitchell. Ridge resonators: impact of excitation beam and resonator losses. *Optics Express*, 29(17):27092–27103, 2021.

[43] M. Hammer, L. Ebers, and J. Förstner. Hybrid coupled mode modelling of the evanescent excitation of a dielectric tube by semi-guided waves at oblique angles. *Optical and Quantum Electronics*, 52:472, 2020.

[44] M. Hammer, L. Ebers, and J. Förstner. Resonant evanescent excitation of guided waves with high-order optical angular momentum. *Journal of the Optical Society of America B*, 38(5):1717–1728, 2021.

[45] M. Hammer, L. Ebers, and J. Förstner. Resonant evanescent excitation of OAM modes in a high-contrast circular step-index fiber. In D. L. Andrews, E. J. Galvez, and H. Rubinsztein-Dunlop, editors, *Complex Light and Optical Forces XVI*, volume 12017, page 120170F. SPIE, 2022.

[46] S. S. M. Khaleghi, P. Karimi, and A. Khavasi. On-chip second-order spatial derivative of an optical beam by a periodic ridge. *Optics Express*, 28(18):26481–26491, 2020.

[47] H. Xu and Y. Shi. Silicon-waveguide-integrated high-quality metagrating supporting bound state in the continuum. *Laser & Photonics Reviews*, 14(6):1900430, 2020.

[48] E. A. Bezus, D. A. Bykov, and L. L. Doskolovich. Total absorption and coherent perfect absorption in metal–dielectric–metal resonators integrated into a slab waveguide. *Optics Letters*, 47(17):4403–4406, 2022.

[49] L. Ebers, M. Hammer, and J. Förstner. Light diffraction in slab waveguide lenses simulated with the stepwise angular spectrum method. *Optics Express*, 28(24):36361–36379, 2020.

[50] F. Çivitci, M. Hammer, and H. J. W. M. Hoekstra. Planar prism spectrometer based on adiabatically connected waveguiding slabs. *Optics Communications*, 365:29–37, 2016.

[51] R. Wang, J. Chen, Y. Xiang, Y. Kuai, P. Wang, H. Ming, J. R. Lakowicz, and D. Zhang. Two-dimensional photonic devices based on Bloch surface waves with one-dimensional grooves. *Physical Review Applied*, 10:024032, 2018.

[52] Y. Augenstein, A. Vetter, B. V. Lahijani, H. P. Herzig, C. Rockstuhl, and M.-S. Kim. Inverse photonic design of functional elements that focus Bloch surface waves. *Light: Science & Applications*, 7:104, 2018.

[53] E. A. Bezus, D. A. Bykov, and L. L. Doskolovich. Integrated diffraction gratings on the Bloch surface wave platform supporting bound states in the continuum. *Nanophotonics*, 10(17):4331–4340, 2021.

[54] E. A. Bezus, D. A. Bykov, L. L. Doskolovich, and E. A. Kadomina. Integrated resonant diffraction gratings for Bloch surface waves. *Optical Memory and Neural Networks*, 31(1):S8–S13, 2022.

[55] M. Hammer, L. Ebers, and J. Förstner. Configurable lossless broadband beam splitters for semi-guided waves in integrated silicon photonics. *OSA Continuum*, 4(12):3081–3095, 2021.

[56] M. Hammer. Oblique incidence of semi-guided waves on rectangular slab waveguide discontinuities: A vectorial QUEP solver. *Optics Communications*, 338:447–456, 2015.

[57] R. Soref. The past, present, and future of silicon photonics. *IEEE Journal of Selected Topics in Quantum Electronics*, 12(6):1678–1687, 2006.

[58] G. T. Reed. *Silicon photonics: the state of the art*. John Wiley & Sons, 2008.

[59] X. Chen, M. M. Milosevic, S. Stanković, S. Reynolds, T. D. Bucio, K. Li, D. J. Thomson, F. Gardes, and G. T. Reed. The emergence of silicon photonics as a flexible technology platform. *Proceedings of the IEEE*, 106(12):2101–2116, 2018.

[60] A. R. Forouhi and I. Bloomer. Optical dispersion relations for amorphous semiconductors and amorphous dielectrics. *Physical Review B*, 34:7018–7026, 1986.

[61] G. E. Jellison and F. A. Modine. Parameterization of the optical functions of amorphous materials in the interband region. *Applied Physics Letters*, 69(3):371–373, 1996.

[62] M. Hammer. OMS — 1-D mode solver for dielectric multilayer slab waveguides. https://www.computational-photonics.eu/oms.html.

[63] I. V. Lindell and A. H. Sihvola. Electromagnetic boundary conditions defined in terms of normal field components. *IEEE Transactions on Antennas and Propagation*, 58(4):1128–1135, 2010.

[64] M. Lohmeyer. Mode expansion modeling of rectangular integrated optical microresonators. *Optical and Quantum Electronics*, 34(5):541–557, 2002.

[65] M. Hammer. METRIC — Mode expansion tools for 2D rectangular integrated optical circuits. https://metric.computational-photonics.eu/.

[66] Comsol Multiphysics GmbH, Göttingen, Germany; http://www.comsol.com.

[67] J. D. Joannopoulos, R. D. Meade, and J. N. Winn. *Photonic Crystals: Molding the Flow of Light*. Princeton, 1995.

[68] A. D. Simard, N. Belhadj, Y. Painchaud, and S. LaRochelle. Apodized silicon-on-insulator Bragg gratings. *IEEE Photonics Technology Letters*, 24(12):1033–1035, 2012.

[69] M. Ma, Z. Chen, H. Yun, Y. Wang, X. Wang, N. A. F. Jaeger, and L. Chrostowski. Apodized spiral Bragg grating waveguides in silicon-on-insulator. *IEEE Photonics Technology Letters*, 30(1):111–114, 2018.

[70] E. Hecht. *Optics*. Pearson Education, 2017.

[71] M. Maksimovic, M. Hammer, and E. van Groesen. Field representation for optical defect microcavities in multilayer structures using quasi-normal modes. *Optics Communications*, 281(6):1401–1411, 2008.

[72] R. Ghosh, K. K. Ghosh, and R. Chakraborty. Narrow band filter using 1D periodic structure with defects for DWDM systems. *Optics Communications*, 289:75–80, 2013.

[73] M. Born and E. Wolf. *Principles of Optics, 7th. ed.* Cambridge University Press, Cambridge, UK, 1999.

[74] A. W. Snyder and J. D. Love. *Optical Waveguide Theory*. Chapman and Hall, London, New York, 1983.

[75] A. Hadij-ElHouati, P. Cheben, A. Ortega-Moñux, J. G. Wangüemert-Pérez, R. Halir, J. de Oliva-Rubio, J. H. Schmid, and I. Molina-Fernández. High-efficiency conversion from waveguide mode to an on-chip beam using a metamaterial engineered Bragg deflector. *Optics Letters*, 46(10):2409–2412, 2021.

[76] Y. Shi, W. Li, A. Raman, and S. Fan. Optimization of multilayer optical films with a memetic algorithm and mixed integer programming. *ACS Photonics*, 5(3):684–691, 2018.